On the Impact of Mechanics on Electrochemistry of Lithium-Ion Battery Anodes

ANKIT VERMA [1,2] AVTAR SINGH [1] and ANDREW COLCLASURE [1]

1.—Energy Conversion and Storage Systems Center, National Renewable Energy Laboratory, Golden, CO 80401, USA. 2.—e-mail: ankit.verma@nrel.gov

Models exploring electrochemistry-mechanics coupling in liquid electrolyte lithium-ion battery anodes have traditionally incorporated stress impact on thermodynamics, bulk diffusive transport, and fracture, while stress-kinetics coupling is more explored in the context of all solid-state batteries. Here, we showcase the existence of strong link between active particle surface pressure and reaction kinetics affecting performance even in liquid electrolyte systems. Traction-free and immobile particle surface mechanical boundary conditions are used to delineate the varying pressure magnitudes in graphite host during cycling. Both tensile and compressive stresses are generated in traction-free case, while a fixed surface subjects the entire particle to a compression state. Pressure magnitudes are nearly two to three orders of magnitude higher for the latter resulting in significant depression of open circuit potential and improvement of exchange current densities compared to stress-free state. The results demonstrate the need for incorporating stress-kinetics linkage in models and provide a rationale for putting battery electrodes under compression to improve kinetics.

INTRODUCTION

Lithium-ion battery (LIB) performance is primarily dictated by particle level dynamics incorporating a complex interplay of coupled interfacial thermodynamics (Li/Li$^+$ open circuit potential), reaction kinetics (Li/Li$^+$ exchange current density), and bulk diffusive transport (Li diffusivity) phenomena.[1] Furthermore, intercalation/alloying of lithium into battery electrodes gives rise to particle-level stresses from concentration gradients (e.g., diffusion-induced stress in lithium manganese oxide, graphite),[2–5] large volume expansion (e.g., phase transformation in silicon),[6–8] and constrained boundary effects (e.g., particle-particle, particle-conductive binder domain, particle-current collector contact, core-shell dynamics).[9,10] Mechanics has a strong coupling to thermodynamics, kinetics, and transport; consequently, we expect stress dynamics to significantly alter LIB electrochemistry.[11,12] In this article, we focus on understanding this coupled stress-electrochemistry paradigm. While previous works have mostly focused on the impact of stress on thermodynamics and solid-phase transport in liquid electrolyte LIBs,[13,14] here we show that stress-reaction kinetics coupling can modify performance as well.

The role of mechanics (stress) on bulk diffusive transport inside the particle and interfacial thermodynamics is relatively well studied for small-strain graphite as well as large deformation silicon anode systems for unconstrained expansion.[15,16] Diffusion-induced stress results in stress-assisted diffusion, which enhances the bulk particle-level Li diffusivity.[17,18] For spherical particles, this is expressed as:

$$\frac{D_s}{D_s^0} = 1 + \theta c, 0 < c < c_s^{\max} \tag{1}$$

$$\theta = \left(\frac{\Omega_{Li}}{RT}\right) \frac{2\Omega E}{9(1-v)} \tag{2}$$

Here, D_s is the bulk phase Li diffusivity of anode particle with lithiation; D_s^0 is the diffusivity at unlithiated stress-free state. Note that nominal diffusivity can be concentration dependent.[19] Lithiation improves diffusivity with the enhancement factor dependent on mechanical properties (Young's modulus E, Poisson's ratio v), molar volume of intercalated lithium, Ω_{Li} and maximum Li concentration inside the particle, c_s^{max}. Figure 1a and b showcases the quantitative trends of mechanical properties and diffusivity factor enhancement dependent on degree of lithiation for graphite and silicon obtained from Eq. 1. Graphite and silicon show stiffening and softening behavior with lithiation respectively, resulting in a threefold increase in Young's modulus for graphite and nearly fourfold decrease in Young's modulus for silicon with full lithiation.[20–22] Poisson's ratio is approximately constant for graphite while it shows a slight increase

for silicon. All mechanical (E, v) and thermodynamic properties (Ω_{Li}, c_s^{max}) of graphite and silicon are obtained from literature and are reported in Table I. The corresponding trends for stress-induced diffusivity enhancement show a $\sim 60\%$ maximum increase in graphite nominal diffusion, while silicon diffusivity can improve up to $\sim 2000\%$ with lithiation, indicating the advantages of stressed state.

Equilibrium potentials are impacted by stress according to:[27]

$$U = U^0 - \frac{\Omega_{Li} p_s}{F} \qquad (3)$$

Here, U and U^0 are the equilibrium potentials in the stressed and relaxed state respectively, and p_s is the surface pressure in the electrode particle. Tensile stresses lead to negative pressure resulting in positive deviation of the open circuit potential (OCP) from stress-free state. Figure 1c shows this
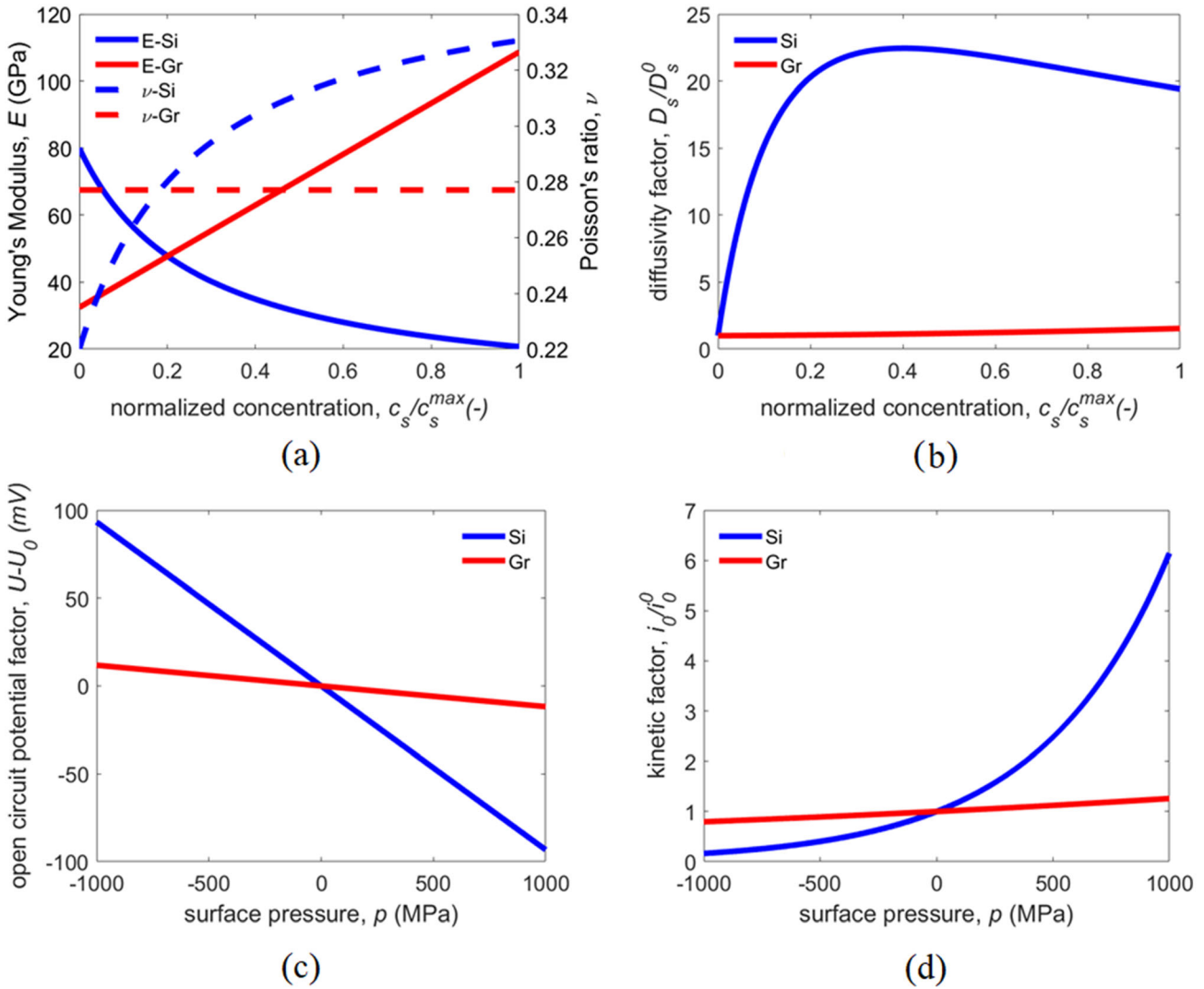

Fig. 1. (a) Variation of Young's modulus and Poisson's ratio for silicon and graphite with normalized lithium content, (b) corresponding diffusivity factor enhancement. Li content varies from 0 to 1 for empty to full lithiation state. (c) Open circuit potential factor variation and (d) exchange current density factor variation with anode particle surface pressure. The pressure range is from $-$ 1 GPa to 1 GPa.

Table I. Silicon and graphite mechanical and thermodynamic property data

Parameter	Graphite	Silicon	Ref
c_s^{max} (mol/m³)	30,900	81,967 (based on final radius), 311,474.6 (based on initial radius)	23–25
Ω_{Li} (m³/mol)	1.14×10^{-6}	9×10^{-6}	3, 25
Ω_{host} (m³/mol)	8.69×10^{-6}	1.2×10^{-5}	25, 26
$E(\bar{c})$ (GPa) $0 < \bar{c} < 1$	$E_i + (E_f - E_i)\bar{c}$ $E_i = 32.47; E_f = 108.67$	$aE_{Li} + (1-a)E_{Si}$ $a = \frac{x_{max}\bar{c}}{x_{max}\bar{c}+1}$ $E_{Li} = 4.91; E_{Si} = 80$	21, 22
$v(\bar{c})$ (–) $0 < \bar{c} < 1$	0.277	$av_{Li} + (1-a)v_{Si}$ $a = \frac{x_{max}\bar{c}}{x_{max}\bar{c}+1}$ $v_{Li} = 0.36; v_{Si} = 0.22$	3, 22
i_0^0 (A/m²)	12 ($\bar{c} = 0.5$)	–	23, 24
D_s^0 (m²/s)	1.6×10^{-14}	–	23, 24
$U^0(V)$ (Gr)	$0.1493 + 0.8493\exp(-61.79\bar{c}) + 0.3824\exp(-665.8\bar{c}) - \exp(39.42\bar{c} - 41.92) - 0.0313\tan^{-1}(25.59\bar{c} - 4.099) - 0.009434\tan^{-1}(32.49\bar{c} - 15.74)$		23, 24

variation of the OCP factor $(U - U^0)$ as a function of the particle surface stress magnitudes. It is evident that the high molar volume of Li in Si can result in large equilibrium potential gap of $\sim$ 93.3 mV at a surface stress state of 1 GPa. The corresponding voltage gap for graphite particle is $\sim$ 11.8 mV at 1 GPa surface pressure. This gap reduces to zero as the particle stress goes to a fully relaxed state. Silicon anodes do exhibit large voltage hysteresis between lithiation and delithiation at low current rates, possibly indicating the persistence of high-stress magnitudes at the particle surface.[28–31] Alternatively, this hysteresis can possibly arise out of slower diffusion/kinetics[28] or multiphase lithiation.[32]

The impact of stress on reaction kinetics is well studied in metal anode-solid electrolyte literature[33,34] but has been largely ignored for intercalation-based liquid electrolyte systems. Recently, Ganser and coworkers have devised a formulation for Butler–Volmer exchange current density incorporating the influence of mechanics.[35] For intercalation particles with concentrated electrolyte theory, this takes the form:

$$i_0 = i_0^0\exp\left(\frac{\alpha}{RT}\Omega_{Li}p_s\right)\exp\left(\frac{(1-\alpha)}{RT}\Omega_{Li^+}p_e\right) \quad (4)$$

Here, i_0, i_0^0 are the stressed and stress-free state exchange current densities, respectively, α is the symmetry factor generally taken to be 0.5, Ω_{Li}, Ω_{Li^+} are the partial molar volumes of intercalated Li in solid host and ionic Li$^+$ ion in the electrolyte phase, respectively, and p_s, p_e are the pressure in the active electrode particle and electrolyte, respectively. In liquid electrolyte systems, fluid pressure is usually negligible if there is extra volume available for the fluid to move in and out while active intercalation particles can experience high stress magnitudes in the MPa to GPa range.[36,37] Figure 1d explores the impact of particle-level surface stresses on the exchange current density factor for graphite and silicon. Compressive stresses of 1 GPa result in $\sim$ 25% and $\sim$ 514% enhancement in reaction kinetics magnitudes for graphite and silicon, respectively, from stress-free state. Conversely, tensile surface stress states of 1 GPa reduce the reaction kinetics by $\sim$ 20% and $\sim$ 84%, respectively, for graphite and silicon. Under traction-free boundary conditions, surface hydrostatic stress state switches from compressive to tensile stresses for lithiation vs delithiation of anode particles.[18] This can lead to increased kinetic overpotentials for Li extraction compared to Li insertion.

For the rest of the article, we focus on understanding the impact of large stresses on graphite performance, which is amenable to small-strain treatment as opposed to silicon. We build a single particle half-cell model for graphite with coupled mechanics-electrochemistry effects to show stress impact of performance.[38] This model solves for Li

concentration and stress in the spherical graphite particle alongside voltage evolution with time.[17,18] Concentration equation and its boundary conditions take the form:

$$\frac{\partial c}{\partial t} = D \left[\frac{\partial^2 c}{\partial r^2} + \frac{2}{r}\frac{\partial c}{\partial r} + \theta \left(\frac{\partial c}{\partial r} \right)^2 + \theta c \left(\frac{\partial^2 c}{\partial r^2} + \frac{2}{r}\frac{\partial c}{\partial r} \right) \right] \quad (5)$$

$$\text{BC} : r = 0, \frac{\partial c}{\partial r} = 0; r = R, -D(1 + \theta c) = \frac{i}{F} \quad (6)$$

Here, c is the Li concentration in the graphite particle and D is nominal stress-free diffusivity. Symmetry boundary condition at the particle center and constant flux boundary condition at the particle surface corresponding to constant current operation are used. For stress solve, two different mechanical boundary conditions are considered for the graphite particle surface: (1) traction-free, radial stress $\sigma_r = 0$ and (2) immobile boundary, displacement $u = 0$. Traction-free boundary condition is representative of the graphite particle being surrounded by soft matrix of conductive binder domain and electrolyte, which is easily displaced by the graphite expansion.[39] Immobile surface is representative of a rigid shell (artificial layer/solid electrolyte interphase) or neighboring particles fully constraining the expansion of the graphite particle.[40,41] For this model, variation of graphite Young's modulus with lithiation is not considered and a fixed mean value of 70.57 GPa is used, which is the average Young's modulus of fully delithiated and lithiated graphite.[3] Constant Young's modulus allows for decoupling the concentration and stress to solve and obtain the analytical form for hydrostatic stress shown below.[17]

For each of the mechanical boundary conditions, the hydrostatic stress magnitude can be derived from the concentration evolution as

$$\text{Traction-free surface} : \sigma_\text{h}(r)$$
$$= \frac{2\Omega_\text{Li}E}{9(1-\upsilon)} \left[\left(\frac{3}{R^3} \int_0^R cr^2 \mathrm{d}r \right) - c \right] \quad (7)$$

Immobile surface :
$$\sigma_\text{h}(r) = \frac{2\Omega_\text{Li}E}{9(1-\upsilon)} \left[\left(-\left(\frac{1+\upsilon}{2(1-2\upsilon)} \right) \frac{3}{R^3} \int_0^R cr^2 \mathrm{d}r \right) - c \right] \quad (8)$$

Here, literature expressions of hydrostatic stress, $\sigma_\text{h}(r)$, for the traction-free boundary condition are utilized[17,18] while quasistatic stress solve with appropriate strain-displacement, stress-strain constitutive relations, and immobile surface boundary conditions is performed to obtain the hydrostatic stress function for the latter case. Note that pressure is just the hydrostatic stress with the sign reversed.

Figure 2a shows the temporal evolution of voltage and current data for a graphite half-cell cycling between 30 mV and 750 mV at a nominal current rate of C/10 for traction-free graphite surface. For the stress-free reference state, graphite OCP, reaction rate constants, and diffusivity are taken from literature and reported in Table I. The corresponding variation of surface pressure, OCP factor, and kinetic factor with time is shown in Fig. 2b and c, respectively. Compressive stresses are generated at the surface during half-cell discharge (graphite lithiation), while tensile stresses are generated at the surface during half-cell charge (graphite delithiation). Pressure magnitude lies in the 5–10 MPa range, which has a negligible impact on the OCP variation magnitudes lying in the ± 0.1 mV range. A similar impact is seen on the kinetic factor with the exchange current densities increasing/decreasing only 0.2–0.3% compared to the stress-free reference exchange current density during lithiation/delithiation, respectively. Figure 2d, e, f and g shows the concentration and pressure profile variation from the particle center to its surface for the first 20 h corresponding to first cycle and slight foray into the second cycle, respectively. Flat concentration profiles during the operation indicate decent diffusive transport at the low C/10 current rates for this 20 μm graphite particle. Stress profiles exhibit the expected transition of surface hydrostatic stresses from compressive to tensile state as we go from lithiation to delithiation. Also, stress transition across the particle radius is observed as we move from the surface to the center of the particle: compressive to tensile transition during lithiation and vice versa during delithiation.

Figure 3b shows the temporal evolution of voltage and current data for a graphite half-cell cycling between 30 mV and 750 mV at a nominal current rate of C/10 for immobile graphite surface. The corresponding time variation of surface pressure, OCP factor, and kinetic factor is shown in Fig. 3b and c respectively. As opposed to the traction free case, here only compressive stresses are generated throughout the cell operation. Pressure magnitude can increase from relaxed state (0 MPa) up to 1000s of MPa range during lithiation, which has a significant impact on depressing the OCP. At the maximum stress levels, the OCP can go down by ~ 20 mV. A similar significant impact is seen on the kinetic factor with the exchange current densities increasing up to 50% near full lithiation compared to the stress-free reference exchange current density. Decrease in OCP could bring the potential of graphite closer to zero during lithiation, which has negative connotations for fast charging as Li plating can happen if the graphite potential drops below 0 V. However, the increase in intercalation exchange current density could be useful in reducing the kinetic overpotentials for the system and delaying plating onset. Figure 3d, e, f and g shows the concentration and pressure profile variation
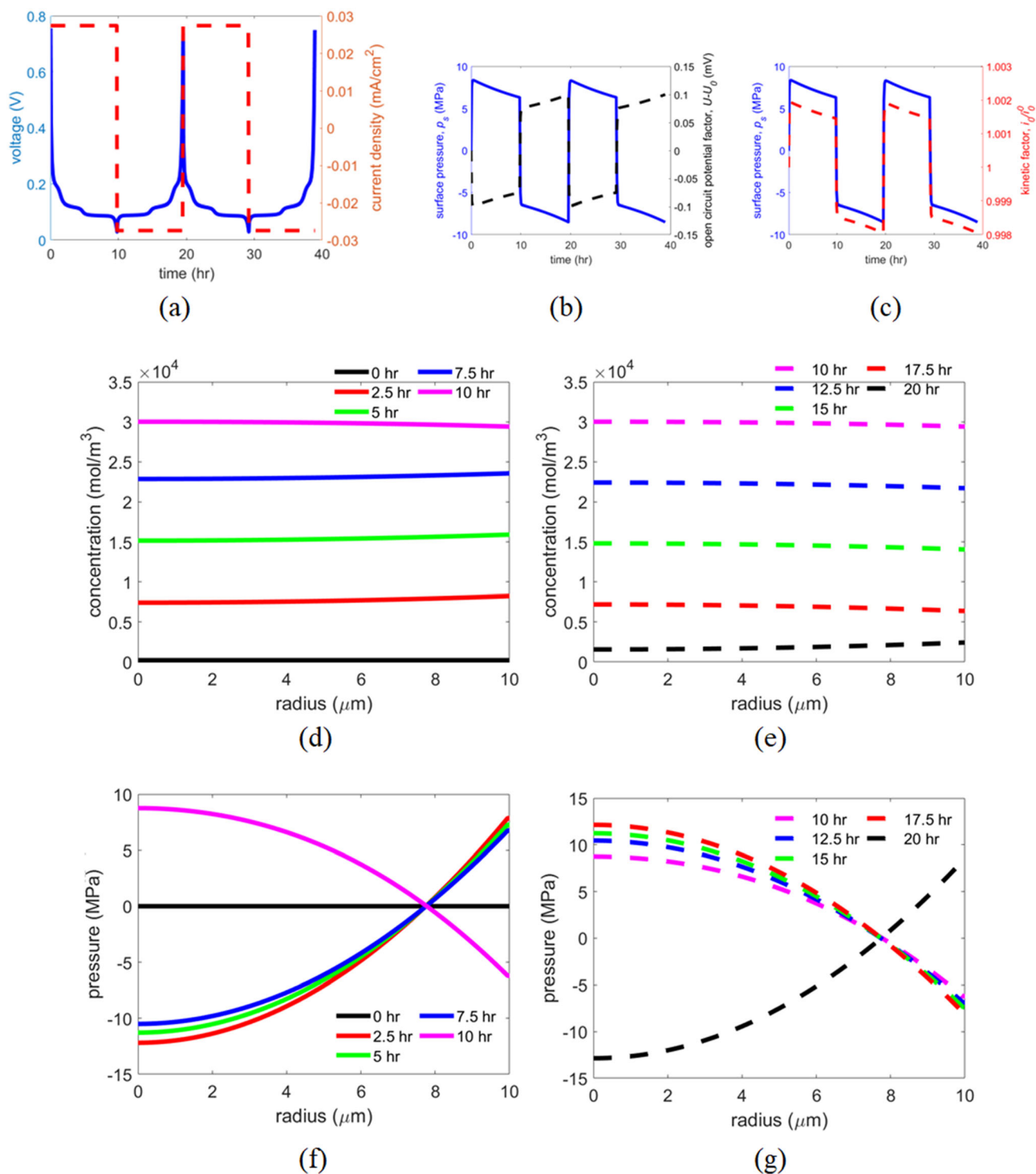
Fig. 2. Graphite particle surface is under traction-free boundary conditions. (a) Voltage and current evolution with time for two cycles between 30 mV and 750 mV at C/10, (b) corresponding surface pressure and open circuit potential factor variation, (c) corresponding kinetic factor variation. (d-e) Concentration variation from particle center to particle surface at different time instants for first 20 h, (f-g) Corresponding pressure variation from particle center to particle surface at different time instants for first 20 h.

from the particle center to its surface for the first 20 h corresponding to first cycle and slight foray into the second cycle, respectively. Flat concentration profiles during the operation indicate good diffusive transport at the low C/10 current rates for this 20-μm graphite particle. All throughout the particle, flat variation of large magnitude compressive stresses is seen. These large compressive stresses can be leveraged to reduce particle fracture as well as improve performance through reduced
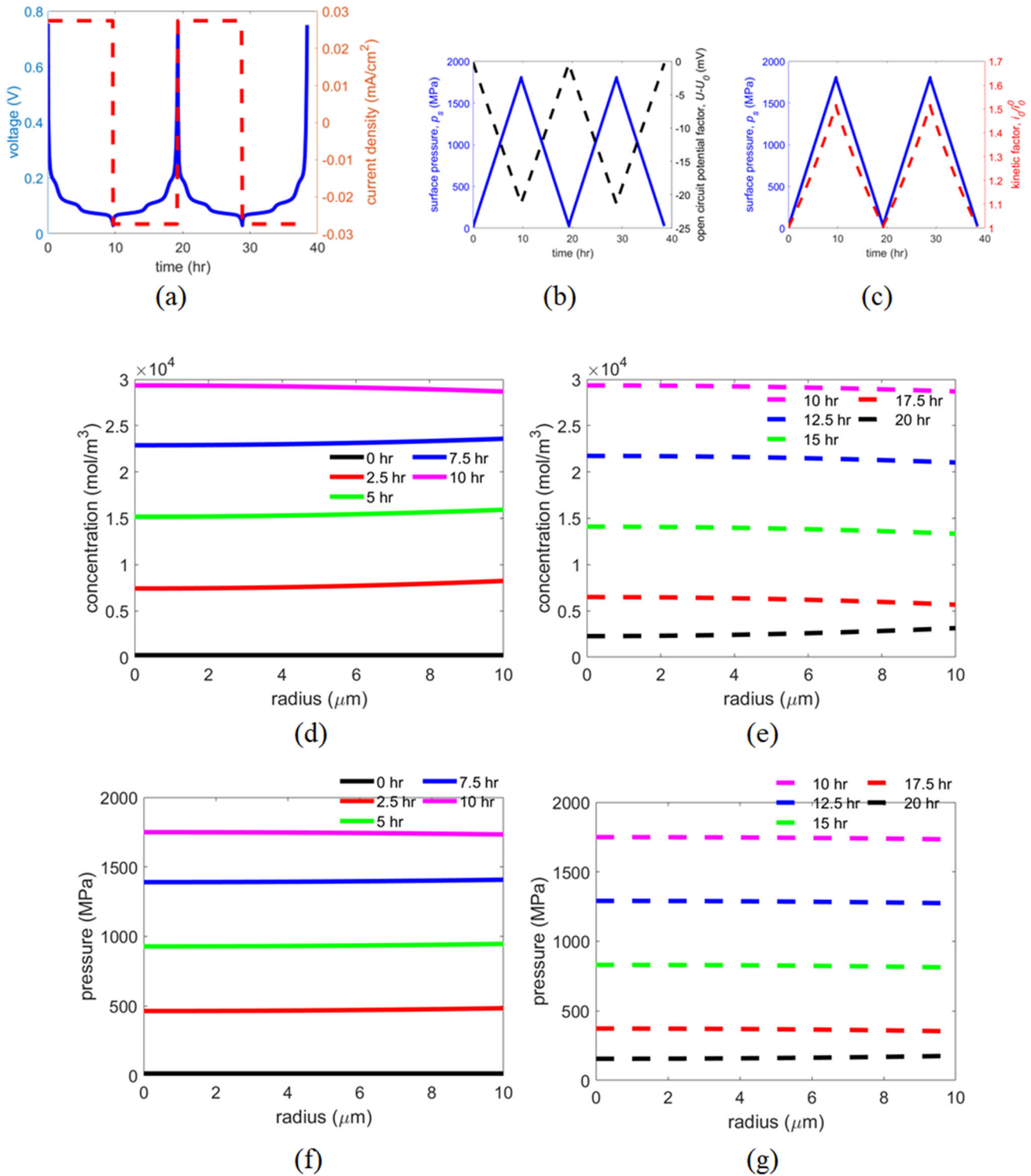
Fig. 3. Graphite particle surface is immobile. (a) Voltage and current evolution with time for two cycles between 30 mV and 750 mV at C/10, (b) corresponding surface pressure and open circuit potential factor variation, (c) corresponding kinetic factor variation. (d-e) Concentration variation from particle center to particle surface at different time instants for first 20 h, (f-g) Corresponding pressure variation from particle center to particle surface at different time instants for first 20 h.

charge transport limitations. Battery electrode particles generally fail through surface crack propagation under tensile stresses; reverting the stress state to compression can be a useful strategy for prolonged operation.[3,42] In literature, pouch cells are subjected to compressive stresses using pressure fixtures, which is hypothesized to improve performance by maintaining good wetting between the
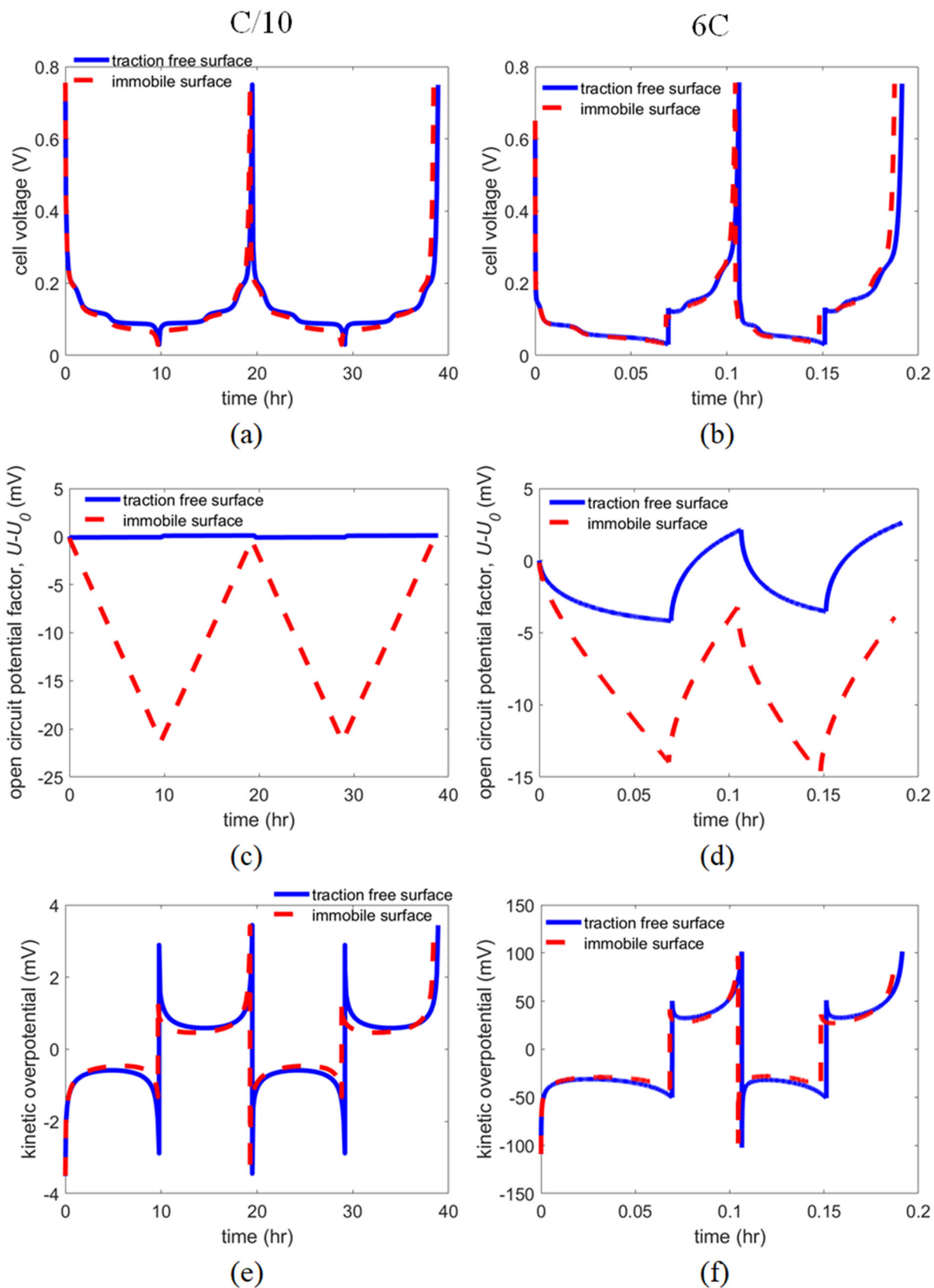
Fig. 4. Comparison of (a-b) cell voltage, (c-d) open circuit potential factor, and (e-f) kinetic overpotential evolution with time for traction-free surface and immobile surface mechanical boundary conditions at C/10 (left panels) and 6C (right panels) rates.

electrode and electrolyte.[43,44] An additional benefit can arise from the analysis showcased here where the resultant compressive stresses can put the entire particle in a state of compression and improve its charge transfer kinetics.

Next, we analyze the impact of current rate on the stress-electrochemistry coupling for the traction-free and immobile graphite particle surface. Figure 4a, b, c and d shows the cell voltage and OCP factor evolution with time, respectively, for traction-free and immobile surface conditions at slow C/10 and fast 6C current rates. At C/10, traction-free surface shows higher voltages than immobile surface (see Fig. 4a) because of large compressive stress generation in the latter which decreases graphite's OCP by up to 20 mV (see Fig. 4c). In comparison, the equilibrium potential is negligibly affected by stress (OCP factor $\sim$ 0 mV) in the traction-free case at C/10. At 6C rate, voltages of traction-free and immobile surface (see Fig. 4b) overlap because even the traction-free surface generates large magnitudes of stress in the 100s of MPa range. This results in maximum $\pm$ 5 mV change in equilibrium potential for traction-free surface versus up to 15 mV OCP reduction for immobile surface (see Fig. 4d). Surface stress magnitude scales with current rate ($\sim$5 MPa at C/10 to $\sim$ 400 MPa at 6C) for the traction-free scenario, leading to more tightly coupled stress-electrochemistry interactions at high magnitude currents. Meanwhile, the immobile surface graphite stress already has 1000s of MPa magnitude at slow C/10 current rate and hence shows relatively less variation with current rate as we go from C/10 to 6C.

Figure 4e and f shows corresponding kinetic overpotential evolution with time for C/10 and 6C for traction-free and immobile graphite particle. Note that kinetic overpotential magnitudes for 6C are drastically higher than C/10 because of the 60-fold increase in current densities. Lowering of overpotential magnitudes for the immobile surface due to exchange current density enhancement from higher stress state is evident for both slow and fast current rates. This is a positive aspect of immobile surface.

CONCLUSION AND OUTLOOK

Diffusion-induced stresses in battery anodes can impact the thermodynamics (open circuit potential), reaction kinetics (exchange current density), and bulk diffusive transport (diffusivity) inside the anode particles. Here, we consider two extreme scenarios of traction-free and immobile particle surface to delineate the pressure magnitude variations in spherical graphite particle and its subsequent impact on electrochemistry. High-magnitude stresses are generated with immobile surface irrespective of current rate of operation which decreases its open circuit potential while enhancing Li intercalation kinetics. Consequently, electrode

compression can improve anode performance. For the traction-free surface, stresses scale with the current rate; hence, a negligible impact of stress-electrochemistry coupling is seen at low current rates (C/10), and it gradually becomes important at higher current rates (6C).

We showcased our analysis for micron-sized spherical particles. Particle morphology will also affect the concentration gradient profile inside the particle and subsequently the stress state at the surface. Nanosizing particles will lower diffusion lengths and concentration gradients inside the particle decreasing stress magnitudes, which will reduce the impact of stress-kinetics coupling.[45] Surface energy also becomes prominent in nano-sized electrodes (increased surface area to volume ratio), which can lower the stress magnitudes. Particle morphologies other than spherical like cylindrical/platelet are also observed in battery anodes.[46,47] Diffusion behavior inside these systems will vary compared to the symmetrical spherical particle, which will impact the stresses generated. Furthermore, practical electrode particles are irregular with inherent surface roughness;[48] these morphologies can show stress concentration at the surface leading to stronger stress-kinetics coupling.

ACKNOWLEDGEMENTS

FUNDING

CONFLICT OF INTEREST

The authors declare that they have no known competing financial interests or personal relationships that could have appeared to influence the work reported in this paper.

OPEN ACCESS

REFERENCES

1. S. Santhanagopalan, Q. Guo, P. Ramadass, and R.E. White, *J. Power. Sources* 156, 620 (2006).
2. J. Christensen and J. Newman, *J. Electrochem. Soc.* 153, A1019 (2006).
3. P. Barai and P.P. Mukherjee, *J. Electrochem. Soc.* 160, A955 (2013).
4. A. Singh and S. Pal, *Int. J. Solids Struct.* 228, 111098 (2021).
5. A. Singh and S. Pal, *J. Mech. Phys. Solids* 163, 104839 (2022).
6. S. Golmon, K. Maute, S.-H. Lee, and M.L. Dunn, *Appl. Phys. Lett.* 97, 15 (2010).
7. A. Verma and P.P. Mukherjee, *J. Electrochem. Soc.* 164, A3570 (2017).
8. D. Cao, T. Ji, A. Singh, S. Bak, Y. Du, X. Xiao, H. Xu, J. Zhu, and H. Zhu, *Adv. Energy Mater.* 13, 2203969 (2023).
9. A. Verma, T. Kotaka, Y. Tabuchi, and P.P. Mukherjee, *J. Electrochem. Soc.* 165, A2397 (2018).
10. M.W. Verbrugge, Y. Qi, D.R. Baker, and Y.T. Cheng, *Adv. Electrochem. Sci. Eng. Electrochem. Eng. Across Scales Mol. Process.* 15, 193 (2015).
11. M. Kim, Z. Yang, and I. Bloom, *J. Electrochem. Soc.* 168, 010523 (2021).
12. W. Mai, A. Colclasure, and K. Smith, *J. Electrochem. Soc.* 166, A1330 (2019).
13. X. Zhang, A.M. Sastry, and W. Shyy, *J. Electrochem. Soc.* 155, A542 (2008).
14. A.M. Korsunsky, T. Sui, and B. Song, *Materials Design* 69, 247 (2015).
15. J. Christensen, *J. Electrochem. Soc.* 157, A366 (2010).
16. Y. Li, K. Zhang, B. Zheng, and F. Yang, *J. Power. Sources* 319, 168 (2016).
17. X. Zhang, W. Shyy, and A.M. Sastry, *J. Electrochem. Soc.* 154, A910 (2007).
18. D. Clerici, F. Mocera, and A. Somà, *Energies* 13, 1717 (2020).
19. M.W. Verbrugge, and B.J. Koch, *J. Electrochem. Soc.* 150, A374 (2003).
20. R. Deshpande, Y. Qi, and Y.-T. Cheng, *J. Electrochem. Soc.* 157, A967 (2010).
21. Y. Qi, H. Guo, L.G. Hector, and A. Timmons, *J. Electrochem. Soc.* 157, A558 (2010).
22. C.V. Di Leo, E. Rejovitzky, and L. Anand, *Int. J. Solids Struct.* 67, 283 (2015).
23. Y. Ji, Y. Zhang, and C.-Y. Wang, *J. Electrochem. Soc.* 160, A636 (2013).
24. B.S. Vishnugopi, A. Verma, and P.P. Mukherjee, *J. Electrochem. Soc.* 167, 090508 (2020).
25. A. Verma, A.A. Franco, and P.P. Mukherjee, *J. Electrochem. Soc.* 166, A3852 (2019).
26. P. Yu, B.N. Popov, J.A. Ritter, and R.E. White, *J. Electrochem. Soc.* 146, 8 (1999).
27. B. Lu, Y. Song, Q. Zhang, J. Pan, Y.-T. Cheng, and J. Zhang, *Phys. Chem. Chem. Phys.* 18, 4721 (2016).
28. R. Chandrasekaran, A. Magasinski, G. Yushin, and T.F. Fuller, *J. Electrochem. Soc.* 157, A1139 (2010).
29. V.A. Sethuraman, M.J. Chon, M. Shimshak, V. Srinivasan, and P.R. Guduru, *J. Power. Sources* 195, 5062 (2010).
30. V.A. Sethuraman, V. Srinivasan, A.F. Bower, and P.R. Guduru, *J. Electrochem. Soc.* 157, A1253 (2010).
31. C. Jin, H. Li, Y. Song, B. Lu, A. Soh, and J. Zhang, *Sci. China Technol. Sci.* 62, 1357 (2019).
32. W. Dreyer, J. Jamnik, C. Guhlke, R. Huth, J. Moškon, and M. Gaberšček, *Nat. Mater.* 9, 448 (2010).
33. C. Monroe and J. Newman, *J. Electrochem. Soc.* 151, A880 (2004).
34. C. Monroe and J. Newman, *J. Electrochem. Soc.* 152, A396 (2005).
35. M. Ganser, F.E. Hildebrand, M. Klinsmann, M. Hanauer, M. Kamlah, and R.M. McMeeking, *J. Electrochem. Soc.* 166, H167 (2019).
36. Z. Zeng, N. Liu, Q. Zeng, S.W. Lee, W.L. Mao, and Y. Cui, *Nano Energy* 22, 105 (2016).
37. M. Wang and X. Xiao, *J. Power. Sources* 326, 365 (2016).
38. M. Guo, G. Sikha, and R.E. White, *J. Electrochem. Soc.* 158, A122 (2010).
39. E.K. Rahani and V.B. Shenoy, *J. Electrochem. Soc.* 160, A1153 (2013).
40. F. Hao and D. Fang, *J. Electrochem. Soc.* 160, A595 (2013).
41. Y. He and H. Hu, *Phys. Chem. Chem. Phys.* 17, 23565 (2015).
42. J.M. Allen, P.J. Weddle, A. Verma, A. Mallarapu, F. Usseglio-Viretta, D.P. Finegan, A.M. Colclasure, W. Mai, V. Schmidt, and O. Furat, *J. Power. Sources* 512, 230415 (2021).
43. A.S. Mussa, M. Klett, G. Lindbergh, and R.W. Lindström, *J. Power. Sources* 385, 18 (2018).
44. L. Zhou, L. Xing, Y. Zheng, X. Lai, J. Su, C. Deng, and T. Sun, *Int. J. Energy Res.* 44, 6778 (2020).
45. R. Deshpande, Y.-T. Cheng, and M.W. Verbrugge, *J. Power. Sources* 195, 5081 (2010).
46. H. Habazaki, M. Kiriu, and H. Konno, *Electrochem. Commun.* 8, 1275 (2006).
47. G. Singh and T.K. Bhandakkar, *Int. J. Mech. Sci.* 163, 105141 (2019).
48. A. Mistry, T. Heenan, K. Smith, P. Shearing, and P.P. Mukherjee, *ACS Energy Lett.* 7, 1871 (2022).